





Slow-down in summer warming over Greenland in the past decade linked to central Pacific El Niño

Shinji Matsumura ¹, Koji Yamazaki ² & Kazuyoshi Suzuki ³

Greenland warming and ice loss have slowed down since the early 2010s, in contrast to the rest of the Arctic region. Both natural variability and anthropogenic forcing contribute to recent Greenland warming by reducing cloud cover and surface albedo, yet most climate models are unable to reasonably simulate the unforced natural variability. Here we show that a simplified atmospheric circulation model successfully simulates an atmospheric teleconnection from the tropics towards Greenland, which accounts for Greenland cooling through an intensified cyclonic circulation. Synthesis from observational analysis and model experiments indicate that over the last decade, more central Pacific El Niño events than canonical El Niño events have generated the atmospheric teleconnection by shifting the tropical rainfall zone poleward, which led to an intensified cyclonic circulation over Greenland. The intensified cyclonic circulation further extends into the Arctic Ocean in observations, whereas the model does not show a direct remote forcing from the tropics, implying the contribution of an indirect atmospheric forcing. We conclude that the frequent occurrence of central Pacific El Niño events has played a key role in the slow-down of Greenland warming and possibly Arctic sea-ice loss.

¹ Faculty of Environmental Earth Science, Hokkaido University, Sapporo, Japan. ² Arctic Research Center, Hokkaido University, Sapporo, Japan. ³ Japan Agency for Marine-Earth Science and Technology, Yokohama, Japan. ✉email: matsusnj@ees.hokudai.ac.jp

Greenland warming is not just regional climate change. The regional warming contributes to global sea-level rise through ice sheet mass loss¹. Recent Greenland warming until 2012 was accelerated by an intensified anticyclone through an atmospheric teleconnection from the tropical Pacific². The intensified anticyclone is associated with the negative phase of the North Atlantic Oscillation (NAO)³, which favours warmer conditions over Greenland and enhances an increase of ice melt by reducing cloud cover and surface albedo during summertime^{4,5}. However, the Greenland warming and ice loss have slowed down over the last decade^{1,6–8}, whereas Arctic warming has continued except for around Greenland (Fig. 1a). This nonuniform Arctic warming can be attributed to natural variability, rather than anthropogenic forcing, although most climate models are unable to reasonably simulate the unforced natural variability over Greenland^{2,9}. In fact, the recent slowdown of the ice loss is suggested to be associated with the phase shift of the NAO¹⁰.

Atmospheric teleconnections connecting the tropics to the Arctic are regarded as a major mechanism for the Arctic natural variability². Most previous studies focus on the impact of winter-time teleconnection on Arctic climate change^{11–14}. In general, tropical ocean variability has a strong influence on higher-latitude atmospheric circulation in winter, as the El Niño–Southern Oscillation (ENSO), which is the leading forcing of extratropical climate variability through generating large scale teleconnection, peaks in boreal winter and is much weaker during boreal summer¹⁵. Nevertheless, recent studies suggest that summer tropical sea surface temperatures (SSTs) can affect Arctic sea ice through an atmospheric teleconnection^{16–20}, although most climate models are unable to reasonably replicate the teleconnection. In summer, however, the subtropical jet is weak and displaced northward, the

westerly ducts (i.e. regions of westerly winds over the equator) is also displaced northwestward, and the easterly winds extend around the equator²¹, which acts to inhibit remote forcing from the tropics^{15,22}. Therefore, it remains unclear how teleconnection propagates from the tropics to the Arctic during summertime. The purpose of the present study is to understand the mechanism of recent slowdown in Greenland warming by focusing on summer-time teleconnection from the tropics. Our study shows that the teleconnection towards Greenland is robust due to the frequent occurrence of central Pacific ENSO, and the observed relationship of Arctic circulation to the central Pacific ENSO is likely to be generated either through indirect forcings or feedbacks.

Results

Recent slow-down in summer warming over Greenland. We first show Greenland temperature anomaly at 700 hPa (~3000 m) in June–August (JJA) (Fig. 1b), which is regarded as an excellent proxy for explaining ice melt variability²³. Greenland warming reaches a peak in 2012, producing new record melt of the Greenland ice sheet, especially in the western coast^{7,24}. However, despite ongoing anthropogenic greenhouse-gas emission, Greenland warming has abruptly slowed down since then (Fig. 1b) and is not evident during the last two decades (Fig. 1a), although ice loss in 2019 is comparable with 2012²⁵. This slowdown of warming over the last decade is observed in surface air temperature (SAT) at several stations along the west coast of Greenland than its east coast⁶, including station Summit located at 3200-m elevation in the centre of Greenland (Supplementary Figure 1). Other reanalysis and reconstruction data also have slight SAT cooling trends in the west side of Greenland over the

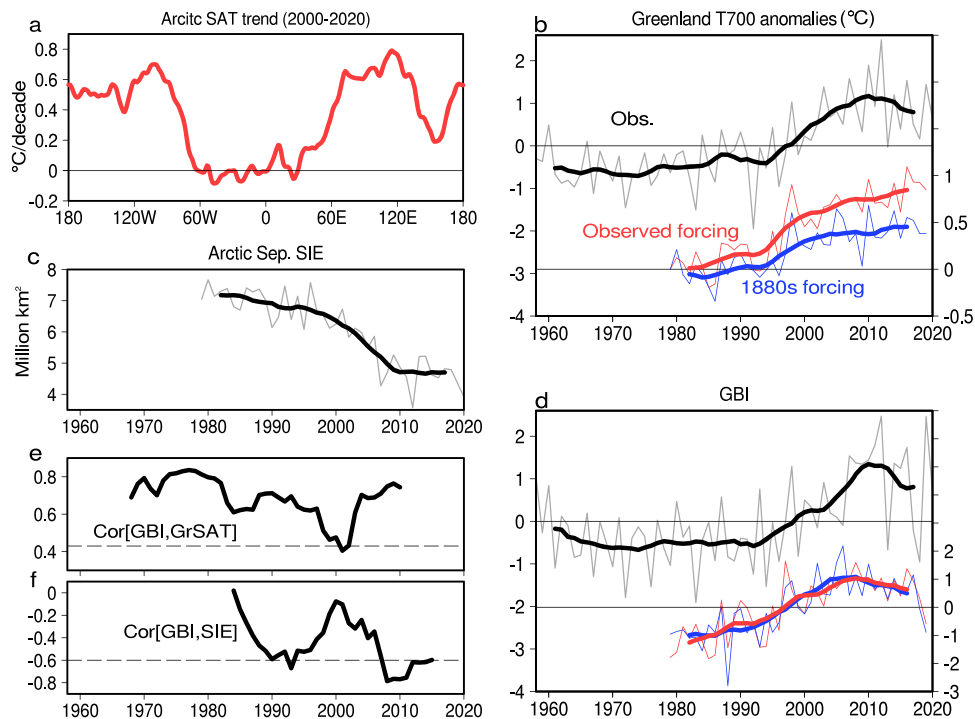


Fig. 1 Recent slow-down in summer warming over Greenland. **a** Longitudinal section of the linear trend of summertime surface air temperature (SAT) averaged over the Arctic (poleward of 60°N) for 2000–2020. Greenland is roughly located at 20°–60°W. **b** Time series of 700-hPa temperature anomaly over Greenland (60°–85°N, 20°–60°W) in JRA55 reanalysis (grey line) for 1958–2020 (anomaly is relative to a climatological mean) and in ECHAM simulations forced by observed (red line) and 1880s (blue line) radiative forcings for 1979–2020 (anomaly is relative to 1979). **c** Time series of Arctic sea ice extent (Million km²) in September. **d** As in **(b)**, but for the Greenland Blocking Index (GBI). Thick lines in **(b)**, **(c)**, and **(d)** denote a smoothed seven-year running mean. **(e)** 21-year running correlation between GBI and Greenland SAT. **(f)** 11-year running correlation between GBI and September Arctic sea-ice extent (SIE). Dashed line denotes the 95% significant level. The correlation is plotted at year 11 (6) of the 21 (11)-year window.

last decade (Supplementary Figure 2). Similar change to Greenland ice loss, the 2012 summer also set new records low of Arctic sea-ice extent (SIE) in September (Fig. 1c). However, no new records have been set since then, although winter maxima have reached record lows²⁶. The pace of Arctic sea ice loss has also slowed down over the last decade^{18,27} (Fig. 1c).

ECHAM5 atmospheric model simulation²⁸ (see Methods) forced with observed radiative forcing accurately reproduces the observed Greenland warming trend from the early 1990s (Fig. 1b), although recent slowdown of warming is absent. Interestingly, the ECHAM5 simulation forced with 1880s radiative forcing also reproduces the warming trend from the early 1990s. The temperature change from 1979 to 2019 is 0.84 °C under the observed forcing and is 0.38 °C under the 1880s forcing, indicating that non-anthropogenic forcing (i.e. atmosphere–ocean natural variability) accounts for about half of recent Greenland warming.

The relationship between Greenland temperature and atmospheric circulation changes can be quantified by the Greenland Blocking Index (GBI) (see Methods). A positive GBI linked to a negative NAO represents stronger anticyclonic circulation over Greenland^{6,9}. Coincident with the temperature anomaly, GBI reaches a peak in 2012 but tends to decrease with large interannual variability afterwards (Fig. 1d), contributing to the recent slowdown of warming. Both simulations also reasonably capture the recent decreased GBI. GBI correlation with Greenland SAT had been robust since the 1960s, but temporarily fell around 2000, and then has rapidly recovered and held robust afterwards (Fig. 1e). GBI correlation with Arctic SIE has also similar changes to that with Greenland SAT since 2000 (Fig. 1f). These results suggest that summer Arctic atmospheric circulation has significantly changed before and after 2000.

Decadal changes in atmospheric teleconnection. The Arctic atmospheric circulation changes before and after 2000 are supported by an empirical orthogonal function (EOF) analysis (see Methods). Figures 2a and b show regressed anomalies of eddy component of 250-hPa geopotential height onto first and second EOF modes over Pacific and Atlantic sectors for 1979–2020 (explaining 15.9% and 12.3% of the total variance, respectively). No significant height anomaly over Greenland is identified in the EOF-1, whereas in the EOF-2 strong negative anomaly is evident in northeastern Canada and Greenland with a centre of action over the Baffin Bay and the Labrador Sea. The EOF-2 pattern represents a Pacific–North America (PNA)-like teleconnection²⁹ combined with a positive NAO² or Pacific–Arctic teleconnection¹⁸, referred to as the non-canonical PNA teleconnection. The first principal component (PC) shows no pronounced trend (Fig. 2c), accounting for the interannual variability of the EOF-1. In contrast, the PC-2 shows a low-frequency variability (Fig. 2d), which corresponds closely to the inverted Greenland temperature and GBI variabilities (Fig. 1b, d), indicating that the EOF-2 represents decadal variability. The EOF-2 pattern with an upward trend over the last decade is related to SAT cooling especially over northeastern Canada and Greenland, North Atlantic SST cooling, and tropical Pacific SST warming (Fig. 2f). The tropical Pacific SST warming pattern shows not canonical eastern Pacific (EP) El Niño, but central Pacific (CP) El Niño, which is characterised by the warmest SST anomalies in the central Pacific^{30,31}. To examine the relation with PCs, we use El Niño Modoki index (EMI)³² as a representative of CP El Niño (see Methods), whereas another index (Niño-4 SST) has also the eastern equatorial Pacific SST warming (Supplementary Figure 3). In the 1980s, EMI correlation with PC-1 was higher than that with PC-2. In the 1990s, however, the EMI correlation with PC-2 rapidly rose

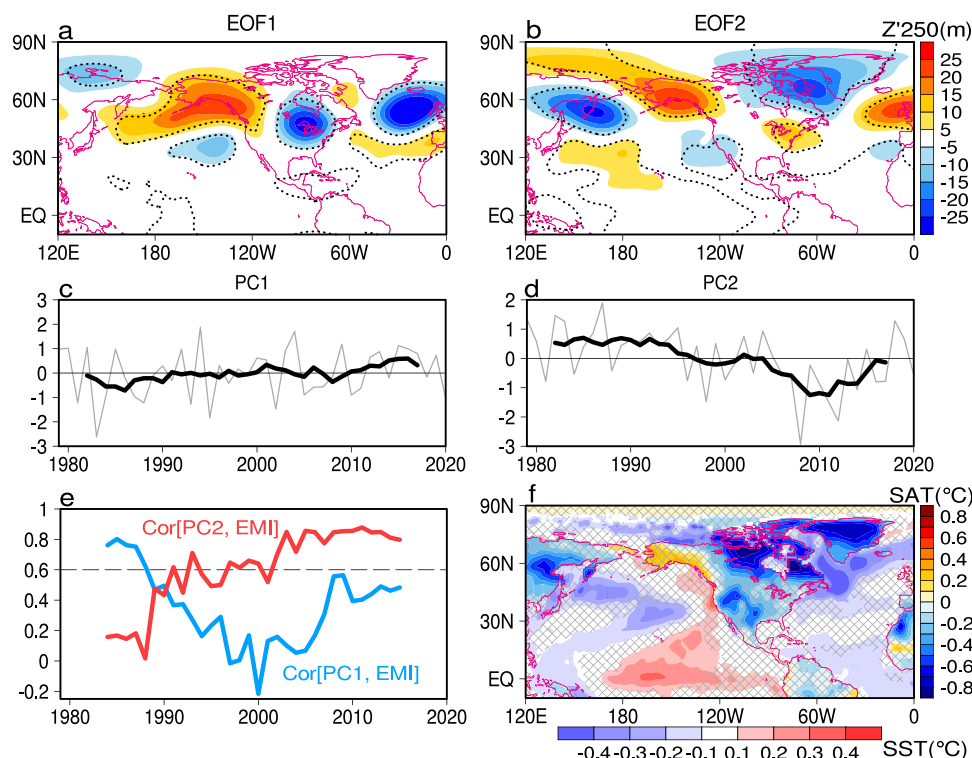


Fig. 2 Major modes of summer tropospheric circulation over Pacific and Atlantic sectors. Regressed anomalies of eddy component of 250-hPa geopotential height onto (a) first and (b) second empirical orthogonal function (EOF) modes, and (c), (d) corresponding principal components (PCs) for 1979–2020, respectively. Dotted contours in (a), (b) indicate the 95% significant level, and thick black lines in (c), (d) indicate 7-year running means. e 11-year running correlations between El Niño Modoki index (EMI) and PC-1 (blue line) and between EMI and PC-2 (red line). Dashed line denotes the 95% significant level. (f) Regressed anomalies of surface air temperature (SAT) over land or ice and sea surface temperature (SST) over open water onto PC-2. Hatching denotes that the anomalies are not statistically significant at the 95% confidence level.

and exceeded that with PC-1 and has held robust since around 2000 (Fig. 2e). In fact, CP El Niño events have occurred more frequently than EP events since the late 1990s^{33–35}, and the tropical SST regression with PC-2 (Fig. 2f) well corresponds to CP El Niño during the recent two decades compared to the earlier decades (Supplementary Figure 3). These results indicate that the contribution of CP El Niño to the EOF-2 pattern has strongly increased since 2000, which is in good agreement with the changes in the relation between Greenland SAT and GBI (Fig. 1e).

Role of central Pacific El Niño. To better understand the role of CP El Niño in the non-canonical PNA teleconnection, we compare the periods before and after 2000. Figures 3a and b show regressed anomalies of detrended 250-hPa geopotential height onto EMI for 1979–1999 and 2000–2020. The earlier decades have no height anomaly over Greenland, resembling the EOF-1 pattern (Fig. 2a), which has a high correlation with EMI in the 1980s (Fig. 2e). In recent decades, wave train pattern propagates from tropical Pacific towards Greenland, consistent with the EOF-2 pattern (Fig. 2b). However, the negative anomaly over Greenland further extends into the Arctic Ocean. In the case of a negative EMI (i.e., CP La Niña), the wave propagation to the Arctic Ocean well corresponds to an intensified anticyclonic circulation trend since 1979³⁶. Overall, teleconnection from the tropics to the Arctic is evident in the recent decades, whereas in the earlier decades, seasonal circulation anomalies are absent in the tropics but are strong over mid-high latitudes with larger internal variability, which might reflect the impact of teleconnection on shorter-term timescale³⁷.

This EMI-related PNA teleconnection is associated with changes in tropical Pacific SST variability. Canonical EP ENSO events

develop in the far eastern Pacific and extend westward during summer, whereas CP ENSO events extend from the eastern subtropics to the central Pacific^{30–32}. Recent SST variability has the largest decrease in the eastern equatorial Pacific, whereas in the subtropical Pacific (i.e. warm pool; 10–20°N) the largest increase occurs (Fig. 3c), supporting stronger CP ENSO than EP ENSO in the recent decades^{33–35}. Precipitation variability also has the largest decrease in the eastern equatorial Pacific and significantly increases at the north of the inter-tropical convergence zone (ITCZ) (Fig. 3d). These changes to SST and precipitation variabilities are also illustrated by comparing the frequency distributions over the eastern subtropical Pacific (Fig. 3e, f). The recent decades (solid line) show a shifted and wider distribution compared to the earlier decades (dashed line), with more frequent or stronger ENSO variability. The shift of the precipitation peak anomaly towards right in the recent decades shows an increase of mean precipitation, whereas mean SST change is much smaller, indicating the importance of CP ENSO variability for the non-canonical PNA teleconnection, such as amplitude and frequency, rather than long-term trend (Supplementary Figure 4). Indeed, EMI-regressed precipitation also increases with a peak at the north of ITCZ in the recent decades, whereas in the earlier decades there is the peak at the south (Fig. 3g and Supplementary Figure 3), resembling the difference between CP and EP El Niños¹⁶.

Over the last decade, CP El Niño was dominant; SST warming is most pronounced in the subtropical Pacific, with increased precipitation at the north of ITCZ (Supplementary Figure 5). When EMI-related component is removed through a simple linear regression analysis, intensified cyclonic circulation and SAT cooling over Greenland mostly disappear (Supplementary Figures 2 and 5), suggesting a critical role of CP El Niño in recent slowdown of Greenland warming.

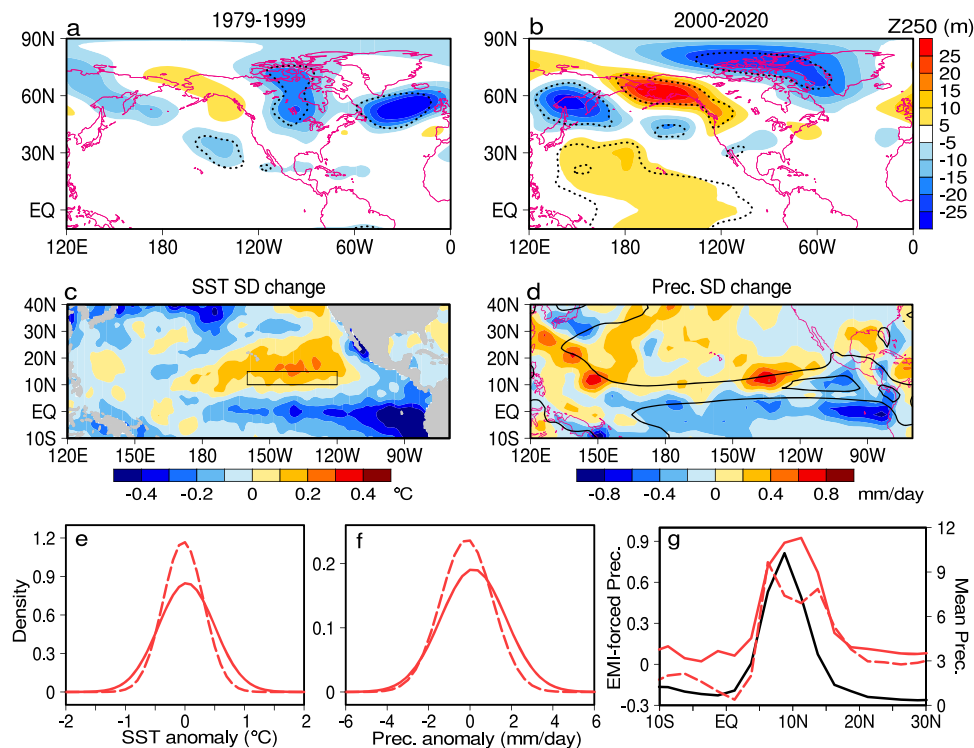


Fig. 3 Decadal changes in central Pacific ENSO teleconnection. Regressed anomalies of detrended 250-hPa geopotential height onto EMI for (a) 1979–1999 and (b) 2000–2020. Dotted contours indicate the 95% significant level. Standard deviation difference between the periods 2000–2020 and 1979–1999 for (c) SST and (d) precipitation. Probability density functions for (e) SST and (f) precipitation anomalies averaged over the eastern tropical Pacific (black rectangle in c; 10°–15°N, 120°–160°W) for the periods 1979–1999 (dashed line) and 2000–2020 (solid line). (g) As in (f), but for meridional section of regressed precipitation anomalies onto EMI. Black contours in d and g indicate mean precipitation (contour interval in (d) is 5 mm day⁻¹).

Simulated teleconnection from the tropics towards Greenland.

To establish the causal relation between CP El Niño and the non-canonical PNA teleconnection, we diagnose atmospheric circulation response to a tropical heating using a linear baroclinic model (LBM) (see Methods). The LBM framework has the distinct advantage that it can isolate the tropical heating impact from extratropical factors. When an idealised heating is centred at 5°N, 120°W, no significant wave train is produced in the upper troposphere (Fig. 4a). When an idealised heating is centred at 15°N under the same longitude, however, the LBM response clearly shows wave-train pattern from tropical Pacific towards Greenland with the positive phase of NAO-like response (Fig. 4b), which is in good qualitative agreement with the EOF-2 (Fig. 2b) and EMI-forced patterns (Fig. 3b). The former heating is located at the south of ITCZ, whereas the latter one is at the north, reflecting precipitation variability before and after 2000, respectively (Fig. 3d, g).

To further ascertain which tropical Pacific region acts as the driving source for the slowdown of Greenland warming and negative circulation anomalies, we systematically examine to set the heating at a 20° interval in longitude and a 5° interval in latitude from the equator to 30°N. Figure 4c and d show 500-hPa geopotential height and 700-hPa temperature responses over Greenland (60°–85°N, 20°–60°W) to the heating whose centre is located at each grid. Strong negative geopotential height responses at 500 hPa over Greenland are identified only at the north of ITCZ peak in the eastern subtropical Pacific (Fig. 4c), roughly consistent with Greenland cooling responses at 700 hPa (Fig. 4d). The sea areas with the pronounced negative height and temperature responses well match those where precipitation

variability shows the largest increase in the recent decades (Fig. 3d). The consistency between model and observed analyses strongly support that the eastern subtropical Pacific is the heating source to drive a Rossby wave to Greenland. In contrast, prior to 2000 when precipitation variability is more active along the south of ITCZ (Fig. 3d), no teleconnection is produced (Fig. 4a).

As noted earlier, ENSO teleconnection is stronger in winter than summer¹⁵. To examine seasonal evolution of Greenland temperature response to a tropical heating, we perform the LBM experiment under the monthly basic state from January to December. Figure 4e and f show seasonal evolution of latitudinal section for 700-hPa Greenland temperature response to a tropical heating at 120°W, and for observed precipitation standard deviation difference between the periods 1979–1999 and 2000–2020 averaged over 120°–160°W, respectively. Strong Greenland cooling is identified along ITCZ in winter and spring, when the eastern tropical Pacific has climatologically westerly winds at the upper troposphere (no hatching in Fig. 4f). Thus, Rossby waves can be generated in this region of westerly winds, leading to Greenland cooling even if precipitation variability is shifted poleward along ITCZ (Fig. 4f). In summer, however, Rossby waves are generally unable to be generated from the eastern tropical Pacific (e.g., Fig. 4a) due to easterly winds across the equator to ITCZ (hatching in Fig. 4f). Nevertheless, more CP events in the recent decades increase precipitation variability at the north of ITCZ with westerly winds (Fig. 4f), which can generate Rossby waves (Fig. 4b) and causes Greenland cooling (Fig. 4d, e). These results suggest that ENSO teleconnections in summer are sensitive to the latitude across ITCZ where atmospheric deep convection is triggered.

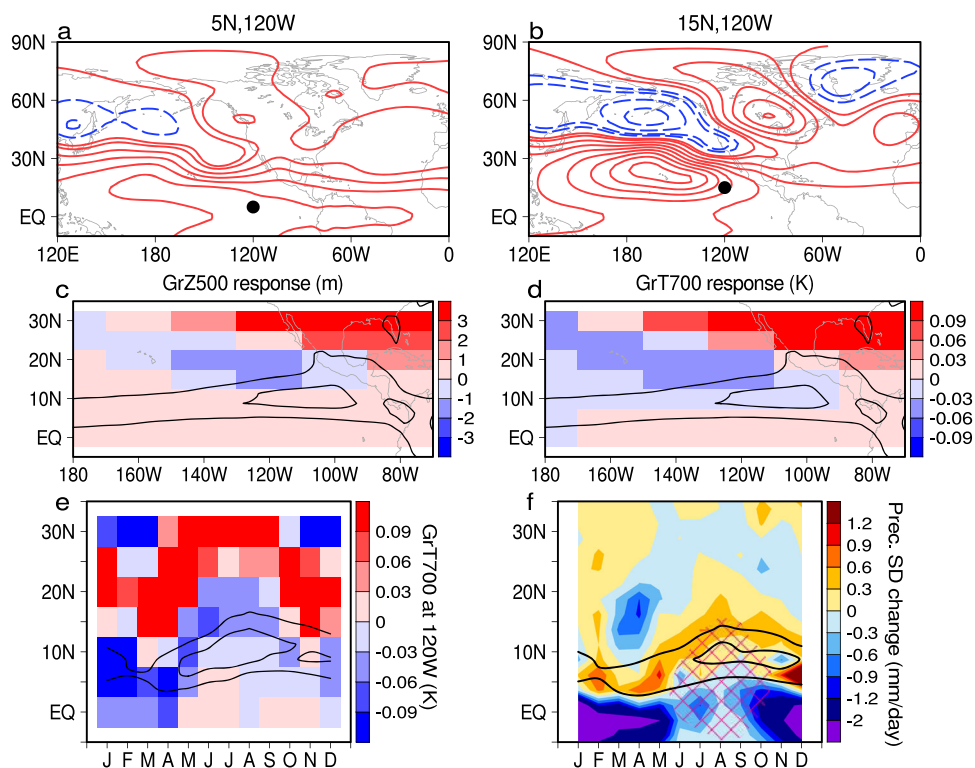


Fig. 4 Simulated teleconnection towards Greenland in response to tropical heating. Response of summertime 250-hPa geopotential height to an idealised heating centred at (a) 5°N, 120°W and (b) 15°N, 120°W (black circles, respectively) in the linear baroclinic model (LBM) experiments (Contours for $\pm 1, \pm 2, \pm 4, \pm 6, \pm 8, \dots$ m; red for positive, blue for negative). Spatial distribution of responses of (c) 500-hPa geopotential height and (d) 700-hPa temperature over Greenland (60°–85°N, 20°–60°W) to a single heating whose centre is located at each grid. Response is plotted at the centre of the heating location. (e) As in (d), but for latitude–time section in response to a heating at 120°W. (f) Latitude–time section of standard deviation difference between the periods 2000–2020 and 1979–1999 for observed precipitation averaged over 120°–160°W. Black contours indicate observed mean precipitation for 1979–2020 (contour interval is 5 mm day⁻¹), and hatching in (f) indicates the regions with easterly at upper troposphere.

In winter, the canonical PNA pattern is dominant over Pacific and North American sectors²⁹. Our LBM experiments in winter reproduce the canonical PNA pattern from the central equatorial Pacific, where rainfall increases during EP El Niño, coexisting with the teleconnection from the eastern equatorial Pacific towards Greenland (Supplementary Figure 6). Meanwhile, the Arctic Oscillation acts as the leading forcing of Arctic climate including Greenland³⁸. The correlation between EMI and GBI for 2000–2020 in winter shows a positive value 0.23, but in summer is -0.42 ($r = -0.43$ at $p = 0.05$), indicating that CP ENSO teleconnection in summer has a stronger influence on Greenland climate variability compared to winter.

Over the last decade, ECHAM5 model also captures the wave-train from the tropical Pacific towards Greenland, where the intensified cyclonic trend disappears when EMI-related component is removed, although the cyclonic trend is shifted westward over eastern Canada, associated with a westward shift of increased tropical Pacific rainfall (Supplementary Figure 7). As a result, recent slowdown of Greenland warming is underestimated in ECHAM5 model compared to observations (Fig. 1b). Another model is also unable to replicate the wintertime teleconnection towards Greenland³⁹. These modelling results suggest that better improvement of tropical rainfall in global model may lead to better behaviour in Arctic climate simulation. Our simple model demonstrates that tropical precipitation variability plays a crucial role in recent summer Greenland climate change.

Possible impact on recent slow-down in Arctic sea-ice loss.

During the last two decades, EMI-induced cyclonic anomalies over Greenland are further extended into the Arctic Ocean

(Fig. 3b), which might affect Arctic sea ice^{16,18–20} through downwelling longwave radiation and ice transport³⁶. Before 2000, sea ice reduction associated with a negative EMI (i.e., CP La Niña) is confined to off the coast of Alaska¹⁶ (Fig. 5a). In the recent two decades, however, the EMI-related sea ice reduction extends to the central Arctic by favouring sea ice transport due to intensified surface anticyclonic circulation (Fig. 5b), well capturing recent Arctic sea-ice loss⁴⁰. Although the sea-ice reduction has slowed down over the last decade^{18,27} associated with intensified cyclonic circulation (Fig. 5c), when EMI-related component is removed, the intensified cyclonic circulation disappears and the sea ice reduction appears to favour in off the coast of Alaska (Fig. 5d). Interestingly, the timing of the abrupt slowdown of September sea ice loss well corresponds to recent upward EMI trend since the late 2000s (Fig. 5e), indicative of the contribution of recent CP El Niño. The interannual correlation between EMI and September SIE is 0.42 ($r = 0.43$ at $p = 0.05$) for 2000–2020 but for 1979–1999 is almost zero, supporting the nonstationary relationship between the subtropical Pacific Ocean and Arctic sea ice²⁰.

While the LBM reproduces the teleconnection towards Greenland, the cyclonic wave amplification to the Arctic Ocean is not found (Fig. 4b). Arctic cyclonic wave responses to tropical heating are identified only at poleward of 25°N within the North Pacific subtropical high, far away from ITCZ (Fig. 5f). Many climate models including ECHAM5 model (Supplementary Figure 7) are also unable to replicate the wave propagation to the Arctic Ocean^{16,18–20}. However, some ensemble members capture well the wave amplification to the Arctic Ocean (see Fig. 10 of ref. 18), implying the contribution of atmospheric internal variability. Our results therefore suggest that the wave propagation to the Arctic Ocean is not caused by a direct remote forcing

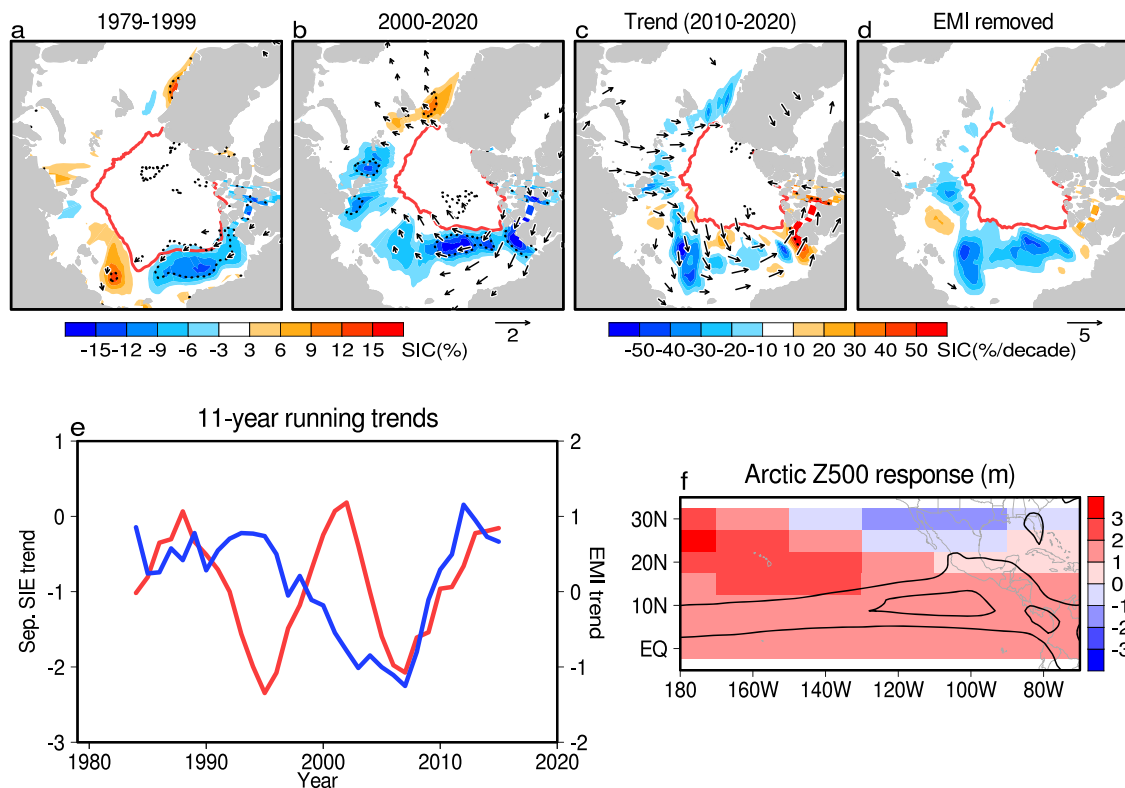


Fig. 5 Relation between recent slowdown in Arctic sea-ice loss and central Pacific ENSO. Regressed anomalies of detrended summertime sea-ice concentration (SIC) (shaded; %) and 10-m wind (vectors; m s^{-1}) onto EMI for (a) 1979–1999 and (b) 2000–2020. c As in (a) and (b), but for linear trends for 2010–2020. d As in (c), but for after removing the EMI-related component. The polarity of EMI is reversed to focus on Arctic sea-ice loss. Dotted contours indicate the 95% significant level, and red contours indicate mean SIC of 90%. (e) Running 11-year trends of EMI (red line) and September SIE (blue line; Million $\text{km}^2/11\text{-year}$). f As in Fig. 4c, but for Arctic response ($70^\circ\text{--}90^\circ\text{N}$, $180^\circ\text{--}60^\circ\text{W}$).

from the tropics, but rather may be amplified by an indirect forcing associated with this teleconnection, such as the North Atlantic SST anomalies⁴¹ (Fig. 2f) and storm tracks⁴².

Discussion

We have successfully simulated summertime teleconnection from the tropics towards Greenland using a simplified atmospheric circulation model. Contrary to the limitation of Rossby waves to propagate poleward in summer, the frequent occurrence of CP El Niño events generates Rossby wave towards Greenland by increasing rainfall at the north of ITCZ with upper tropospheric westerlies, resulting in recent slowdown of Greenland warming. We conclude that CP ENSO teleconnection plays a key role in recent summer Arctic climate change. Most coupled atmosphere–ocean models underestimate recent Greenland warming^{2,9} and faster Arctic sea ice decline after 2000^{43,44}, lacking in the capability to simulate natural variability³⁶, which increases the uncertainties in future projections. Our results here provide important implications for improving Arctic climate simulation. Considering the results of ECHAM5 model forced with observed SST, it seems that natural variability plays a more dominant role in Greenland temperature variability rather than anthropogenic forcing so far. However, it is unclear whether recent frequent CP ENSO is part of natural variability or a consequence of anthropogenic climate change³⁰, as the CP-to-EP ENSO intensity ratio is projected to increase under global warming scenarios⁴⁵. Recent Arctic climate change due to CP ENSO teleconnection might also be a consequence of the interaction between natural variability and anthropogenic forcing¹². Better understanding of tropical and Arctic teleconnections provides an improved understanding of Greenland warming behaviour and Arctic sea-ice loss in a changing climate and may help better improve future projections on the Arctic cryosphere.

Methods

Observational data and analyses. Atmospheric data are from the Japanese 55-year reanalysis (JRA55)⁴⁶. SST and sea-ice concentration data are obtained from the Hadley Centre Global Sea Ice and Sea Surface Temperature (HadISST)⁴⁷. Northern Hemisphere sea ice extent is acquired from the National Snow and Ice Data Centre⁴⁸. Precipitation data are from the Global Precipitation Climatology Project (GPCP)⁴⁹. Greenland surface air temperature data are from Danish Meteorological Institute (DMI) synoptic stations⁵⁰. Terrestrial surface air temperature trend data are also from the Global Historical Climatology Network version 2 and the Climate Anomaly Monitoring System (GHCN CAMS)⁵¹, and from the European Centre for Medium-Range Weather Forecasts (ECMWF) ERA5 reanalysis⁵². Greenland Blocking Index (GBI) is defined as the area-weighted mean 500-hPa geopotential height field calculated over 60°–80°N, 20°–80°W^{6,9}. As a representative of CP El Niño, we use El Niño Modoki index (EMI)³², defined as the difference between SST anomaly averaged over the central Pacific (10°S–10°N, 165°E–140°W) and SST anomaly averaged over the western (10°S–20°N, 125°E–145°E) and eastern (15°S–5°N, 110°–70°W) Pacific.

This study focuses on June–August (JJA). To determine the major modes of upper tropospheric circulation variations, we performed an empirical orthogonal function (EOF) analysis of eddy component of 250-hPa geopotential height over Pacific and Atlantic sector (0°–90°N, 140°E–20°W) for 1979–2020. Before the EOF analysis, geopotential height anomaly data were weighted by the cosine of latitude to ensure that equal areas were afforded equal weight in the analysis. To extract the eddy component of the geopotential height anomaly, the zonal mean component was removed, as EP ENSO leads to a zonally symmetric circulation in the tropics and extratropics^{16,53}. To examine interdecadal variations, we performed running correlation after linear detrending. The significance test used in this study is a standard two-tailed *t*-test with degrees of freedom based on number of years.

Ensemble simulations. We used the Facility for Weather and Climate Assessments (FACTS)²⁸, which is AMIP-type experiment data developed at the NOAA Physical Sciences Laboratory (PSL). We have used a 50-member ensemble mean with the ECHAM5 model for 1979–2019. Two experimental forcings are selected in this study; (1) observed radiative forcing and SST, and (2) 1880s radiative forcing and SST has been detrended and adjusted to 1880 equivalent mean conditions.

LBM experiments. Atmospheric response to a prescribed diabatic heating was calculated by the LBM⁵⁴ with a given climatological basic state and a thermal

forcing. A detailed description of the LBM is found in ref. ⁵⁴. We here used a spectral resolution of T42 with 20 vertical layers. The vertical maximum of the idealised heating (1 K day^{−1}) is placed at 500 hPa, and the half-width of the horizontal heating pattern is 20° in longitude and 6° in latitude⁵⁵. The basic state is based on monthly climatology (averaged 1979–2010) from the National Centres for Environmental Prediction–National Centre for Atmospheric Research (NCEP–NCAR) reanalysis⁵⁶. The experiments are as follows:

- (1) An experiment was performed under a single heating whose centre is located at a certain grid, such as 5°N, 120°W.
- (2) We repeated the experiment (1) at a 20° interval in longitude and a 5° interval in latitude from the equator to 30°N.
- (3) We performed the experiment (2) under the monthly basic state from January to December.

Although the response to the diabatic heating grows with time, the response pattern does not change much after 10 days. The LBM responses in this study are based on 30th day.

Data availability

All data used in this study are publicly available and can be downloaded from the corresponding websites (the JRA55 reanalysis: https://jra.kishou.go.jp/JRA-55/index_en.html; GPCP: <https://www.esrl.noaa.gov/psd/data/gridded/data.gpcp.html>; GHCN CAMS: <https://psl.noaa.gov/data/gridded/data.gncams.html>; ERA5: <https://cds.climate.copernicus.eu/cdsapp#!/home>; HadISST: <https://www.metoffice.gov.uk/hadobs/hadisst/>; Sea ice index: https://nsidc.org/data/seaiice_index/; FACTS: <http://www.esrl.noaa.gov/psd/repository/alias/facts/>).

Code availability

The analysis codes are available from the corresponding author upon reasonable request. All graphics were produced using GrADS version 2.1.0 (<http://cola.gmu.edu/grads/>).

Received: 21 July 2021; Accepted: 30 November 2021;

Published online: 16 December 2021

References

1. The IMBIE Team., et al. Mass balance of the Greenland Ice Sheet from 1992 to 2018. *Nature* **579**, 233–239 (2020).
2. Ding, Q. H. et al. Tropical forcing of the recent rapid Arctic warming in northeastern Canada and Greenland. *Nature* **509**, 209–212 (2014).
3. Hurrell, J. W. Decadal trends in the North Atlantic Oscillation: regional temperatures and precipitation. *Science* **269**, 676–679 (1995).
4. Hofer, S., Tedstone, A. J., Fettweis, X. & Bamber, J. L. Decreasing cloud cover drives the recent mass loss on the Greenland Ice Sheet. *Sci. Adv.* **3**, e1700584 (2017).
5. Lewis, G. et al. Atmospheric blocking drives recent albedo change across the western Greenland ice sheet percolation zone. *Geophys. Res. Lett.* **48**, e2021GL092814 (2021).
6. Hanna, E. et al. Greenland surface air temperature changes from 1981 to 2019 and implications for ice-sheet melt and mass-balance change. *Int J Climatol.* **1–17** (2020).
7. Khazendar, A. et al. Interruption of two decades of Jakobshavn Isbrae acceleration and thinning as regional ocean cools. *Nat. Geosci.* **12**, 277–283 (2019).
8. Mougnot, J. et al. Forty-six years of Greenland Ice Sheet mass balance from 1972 to 2018. *Proceedings of the National Academy of Sciences* **116**, 9239–9244 (2019).
9. Hanna, E., Fettweis, X. & Hall, R. J. Brief communication: recent changes in summer Greenland blocking captured by none of the CMIP5 models. *The Cryosphere* **12**, 3287–3292 (2018).
10. Bevis, M. et al. Accelerating changes in ice mass within Greenland, and the ice sheet's sensitivity to atmospheric forcing. *Proceedings of the National Academy of Sciences* **116**, 1934–1939 (2019).
11. Lee, S., Gong, T., Johnson, N., Feldstein, S. & Pollard, D. On the possible link between tropical convection and the Northern Hemisphere Arctic surface air temperature change between 1958–2001. *J. Clim.* **24**, 4350–4367 (2011).
12. Matsumura, S. & Kosaka, Y. Arctic-Eurasian climate linkage induced by tropical ocean variability. *Nat. Commun.* **10**, 3441 (2019).
13. Li, Z. et al. Different effects of two ENSO types on Arctic surface temperature in boreal winter. *J. Clim.* **32**, 4943–4961 (2019).
14. Matsumura, S., Yamazaki, K. & Horinouchi, T. Robust asymmetry of the future Arctic polar vortex is driven by tropical Pacific warming. *Geophys. Res. Lett.* **48**, e2021GL093440 (2021).
15. Coumou, D. et al. The influence of Arctic amplification on mid-latitude summer circulation. *Nat. Commun.* **9**, 2959 (2018).

16. Hu, C. et al. Shifting El Niño inhibits summer Arctic warming and Arctic sea-ice melting over the Canada Basin. *Nat. Commun.* **7**, 11721 (2016).
17. Meehl, G. A., Chung, C. T. Y., Arblaster, J. M., Holland, M. M. & Bitz, C. M. Tropical decadal variability and the rate of Arctic sea ice decrease. *Geophys. Res. Lett.* **45**, 11326–11333 (2018).
18. Baxter, I. et al. How tropical Pacific surface cooling contributed to accelerated sea ice melt from 2007 to 2012 as ice is thinned by anthropogenic forcing. *J. Clim.* **32**, 8583–8602 (2019).
19. Topál, D. et al. An internal atmospheric process determining summertime Arctic sea ice melting in the next three decades: lessons learned from five large ensembles and multiple CMIP5 climate simulations. *J. Clim.* **33**, 7431–7454 (2020).
20. Bonan, D. B. & Blanchard-Wrigglesworth, E. Nonstationary teleconnection between the Pacific Ocean and Arctic Sea Ice. *Geophys. Res. Lett.* **47**, e2019GL085666 (2020).
21. Ortega, S., Webster, P. J., Toma, V. & Chang, H.-R. The effect of potential vorticity fluxes on the circulation of the tropical upper troposphere. *Q. J. R. Meteorol. Soc.* **144**, 848–860 (2018).
22. Schubert, S., Wang, H. & Suarez, M. Warm season subseasonal variability and climate extremes in the Northern Hemisphere: The role of stationary Rossby waves. *J. Clim.* **24**, 4773–4792 (2011).
23. Fettweis, X. et al. Brief communication “Important role of the mid-tropospheric atmospheric circulation in the recent surface melt increase over the Greenland ice sheet”. *The Cryosphere* **7**, 241–248 (2013).
24. Tedesco, M. et al. Evidence and analysis of 2012 Greenland records from spaceborne observations, a regional climate model and reanalysis data. *The Cryosphere* **7**, 615–630 (2013).
25. Tedesco, M. & Fettweis, X. Unprecedented atmospheric conditions (1948–2019) drive the 2019 exceptional melting season over the Greenland ice sheet. *The Cryosphere* **14**, 1209–1223 (2020).
26. Francis, J. A. & Wu, B. Why has no new record-minimum Arctic sea-ice extent occurred since September 2012? *Environ. Res. Lett.* **15**, 114034 (2020).
27. Swart, N., Fyfe, J. C., Hawkins, E., Kay, J. E. & Jahn, A. Influence of internal variability on Arctic sea-ice trends. *Nat. Clim. Change* **5**, 86–89 (2015).
28. Murray, D. et al. Facility for Weather and Climate Assessments (FACTS): A Community Resource for Assessing Weather and Climate Variability. *Bull. Amer. Meteor. Soc.* **101**, E1214–E1224 (2020).
29. Wallace, J. M. & Gutzler, D. S. Teleconnections in the geopotential height field during the Northern Hemisphere winter. *Mon. Weather Rev.* **109**, 784–812 (1981).
30. Capotondi, A. et al. Understanding ENSO diversity. *Bull. Amer. Meteor. Soc.* **96**, 921–938 (2015).
31. Yeh, S.-W. et al. ENSO atmospheric teleconnections and their response to greenhouse gas forcing. *Reviews of Geophysics* **56**, 185–206 (2018).
32. Ashok, K., Behera, S. K., Rao, S. A., Weng, H. & Yamagata, T. El Niño Modoki and its possible teleconnection. *J. Geophys. Res.* **112**, C11007 (2007).
33. Lee, T. & McPhaden, M. J. Increasing intensity of El Niño in the central–equatorial Pacific. *Geophys. Res. Lett.* **37**, L14603 (2010).
34. Wills, R. C., Schneider, T., Wallace, J. M., Battisti, D. S. & Hartmann, D. L. Disentangling global warming, multidecadal variability, and El Niño in Pacific temperatures. *Geophys. Res. Lett.* **45**, 2487–2496 (2018).
35. Freund, M. B. et al. Higher frequency of Central Pacific El Niño events in recent decades relative to past centuries. *Nat. Geosci.* **12**, 450–455 (2019).
36. Ding, Q. H. et al. Influence of high-latitude atmospheric circulation changes on summertime Arctic sea ice. *Nat. Clim. Change* **7**, 289–295 (2017).
37. Rudeva, I., & Simmonds, I. (2021). Midlatitude Winter Extreme Temperature Events and Connections with Anomalies in the Arctic and Tropics, *Journal of Climate*, **34**, 3733–3749.
38. Wallace, J. M. & Thompson, D. W. J. Annular modes and climate prediction. *Phys. Today* **55**, 28–33 (2002).
39. McCrystall, M. R., Hosking, J. S., White, I. P. & Maycock, A. C. The impact of changes in tropical sea surface temperatures over 1979–2012 on Northern hemisphere high latitude climate. *J. Clim.* **33**, 5103–5121 (2020).
40. Matsumura, S., Zhang, X. & Yamazaki, K. Summer Arctic atmospheric circulation response to spring Eurasian snow cover and its possible linkage to accelerated sea ice decrease. *J. Clim.* **27**, 6551–6558 (2014).
41. Castruccio, F. S. et al. Modulation of Arctic Sea ice loss by atmospheric teleconnections from Atlantic multidecadal variability. *J. Clim.* **32**, 1419–1441 (2019).
42. Wang, S., Chen, W., Chen, S. & Ding, S. Interdecadal change in the North Atlantic storm track during boreal summer around the mid-2000s: role of the atmospheric internal processes. *Clim Dyn.* **55**, 1929–1944 (2020).
43. Notz, D. et al. Arctic Sea ice in CMIP6. *Geophys. Res. Lett.* **47**, e2019GL086749 (2020).
44. Shu, Q. et al. Assessment of sea ice extent in CMIP6 with comparison to observations and CMIP5. *Geophys. Res. Lett.* **47**, e2020GL087965 (2020).
45. Kim, S. T. & Yu, J.-Y. The two types of ENSO in CMIP5 models. *Geophys. Res. Lett.* **39**, L11704 (2012).
46. Kobayashi, S. et al. The JRA-55 Reanalysis: general specifications and basic characteristics. *J. Meteor. Soc. Japan* **93**, 5–48 (2015).
47. Rayner, N. A. et al. Global analyses of sea surface temperature, sea ice, and night marine air temperature since the late nineteenth century. *J. Geophys. Res.* **108**, D144407 (2003).
48. Fetterer, F., Knowles, K., Meier, W. N., Savoie, M. & Windnagel, A. K. updated daily. Sea Ice Index, Version 3. [Indicate subset used]. Boulder, Colorado USA. NSIDC: National Snow and Ice Data Center. <https://doi.org/10.7265/N5K072F8>. [Date Accessed] (2017).
49. Huffman, G. J., Adler, R. F., Bolvin, D. T. & Gu, G. Improving the global precipitation record: GPCP version 2.1. *Geophys. Res. Lett.* **36**, L17808 (2009).
50. Cappelen, J. (Ed.). Greenland – DMI Historical Climate Data Collection 1784–2019. DMI Report 20-04. Copenhagen: Danish Meteorological Institute. <https://www.dmi.dk/publikationer/> (2020).
51. Fan, Y. & van den Dool, H. A global monthly land surface air temperature analysis for 1948–present. *J. Geophys. Res.* **113**, D01103 (2008).
52. Hersbach, H. et al. The ERA5 global reanalysis. *Q. J. R. Meteorol. Soc.* **146**, 1999–2049 (2020).
53. Ding, Q. H., Wang, B., Wallace, J. M. & Branstator, G. Tropical–extratropical teleconnections in boreal summer: observed interannual variability. *J. Clim.* **24**, 1878–1896 (2011).
54. Watanabe, M. & Kimoto, M. Atmosphere–ocean thermal coupling in the North Atlantic: a positive feedback. *Q. J. R. Meteorol. Soc.* **126**, 3343–3369 (2000).
55. Yamazaki, K., Nakamura, T., Ukita, J. & Hoshi, K. A tropospheric pathway of the stratospheric oscillation (QBO) impact on the boreal winter polar vortex. *Atmos. Chem. Phys.* **20**, 5111–5127 (2020).
56. Kalnay, E. et al. The NCEP/NCAR 40-Year Reanalysis Project. *Bull. Amer. Meteor. Soc.* **77**, 437–471 (1996).

Acknowledgements

S.M. was supported by the Grant for Joint Research Programme of the Japan Arctic Research Network Centre. K.S. was supported in part by the JSPS KAKENHI (No.19H05668 and No.16K00581) and ArcS II: Arctic Challenge for Sustainability II, Programme Grant Number JPMXD142031886. We wish to thank J. Cappelen for providing DMI station data.

Author contributions

S.M. conceived the research, analysed the data, and wrote the manuscript with feedback from K.Y. and K.S.; K.Y. designed and performed the LBM experiments. K.S. contributed to analyse the data.

Competing interests

The authors declare no competing interests.

Additional information

Supplementary information The online version contains supplementary material available at <https://doi.org/10.1038/s43247-021-00329-x>.

Correspondence and requests for materials should be addressed to Shinji Matsumura.

Peer review information *Communications Earth & Environment* thanks Irina Rudeva and the other, anonymous, reviewer(s) for their contribution to the peer review of this work. Primary Handling Editor: Heike Langenberg.

Reprints and permission information is available at <http://www.nature.com/reprints>

Publisher's note Springer Nature remains neutral with regard to jurisdictional claims in published maps and institutional affiliations.



Open Access This article is licensed under a Creative Commons Attribution 4.0 International License, which permits use, sharing, adaptation, distribution and reproduction in any medium or format, as long as you give appropriate credit to the original author(s) and the source, provide a link to the Creative Commons license, and indicate if changes were made. The images or other third party material in this article are included in the article's Creative Commons license, unless indicated otherwise in a credit line to the material. If material is not included in the article's Creative Commons license and your intended use is not permitted by statutory regulation or exceeds the permitted use, you will need to obtain permission directly from the copyright holder. To view a copy of this license, visit <http://creativecommons.org/licenses/by/4.0/>.

© The Author(s) 2021